The directional sensitivity of the acoustic radiation force to particle diameter

W. Ran and J. R. Saylor[a)]
Department of Mechanical Engineering, Clemson University, Clemson, South Carolina 29634, USA

(Received 11 September 2014; revised 15 April 2015; accepted 22 April 2015)

When viscous corrections to the inviscid acoustic radiation force theory are implemented and applied to a standing wave field, the direction of the acoustic radiation force on particles varies from theory to theory. Specifically, some theories predict that the direction of the force depends on the particle diameter, while others reveal that the direction of the force is independent of particle diameter. The present study is an experimental investigation of the direction of the acoustic radiation force which suggests that particle diameter does affect the direction. Experiments were conducted in air using an ultrasonic standing wave field with a nominal frequency of 30 kHz. Smoke particles and fine water droplets having a range of diameters were flowed into the region of a standing wave field. The direction of the acoustic radiation force was determined by observing whether the particles accumulated in the nodes or the anti-nodes of the standing wave. Results show a change in the direction of the acoustic radiation force at a particle diameter of $0.3 \pm 0.1\,\mu$m, which corresponds to a particle diameter to acoustic-boundary-layer thickness ratio of 0.023 ± 0.008.
 [http://dx.doi.org/10.1121/1.4921296]

[MFH] Pages: 3288–3298

I. INTRODUCTION

The acoustic radiation force is generated by the interaction between an acoustic field and an object in that field. This force exists for objects of any size, but typical studies involve the interaction with objects having a size smaller than the acoustic wavelength. Many studies involve ultrasonics in either air or water where the wavelength is on the order of a centimeter, or much smaller, and therefore the objects of interest are particles. As shown below, the motivation of the present work is to determine if the sign of this force changes with particle diameter, something which existing theories disagree on. While motivation for the present work is fundamental in nature, we note that many applications exist that will benefit from this work. These include noncontact manipulation of particles such as in cell trapping,[1–3] containerless processing of materials,[4–6] particle/cell sorting,[7–9] and particulate pollution control.[10] This work will also find application in the area of acoustic levitation in general.[11–21,51] We note that in the following development we refer to "particles," however, the theory presented applies equally well to particles and drops and indeed we study both in the experiments presented herein.

Development of theories for the acoustic radiation force dates back to the work of King,[22] which was further developed by Gor'kov[23] to accommodate arbitrary acoustic fields and by Yosioka and Kawasima[24] and Hasegawa and Yosioka[25] to calculate the force on compressible particles. Crum[26] computed and experimentally confirmed a theory for a liquid drop, where compressible and incompressible terms must be included. These theories all utilized the inviscid fluid assumption and so dissipation of the acoustic radiation force was neglected. This assumption is reasonable only when the particle size is much larger than the thickness of the acoustic boundary layer, δ,[27,28]

$$\delta = \sqrt{\frac{2\nu}{\omega}}, \tag{1}$$

where ν is the kinematic viscosity of the surrounding fluid medium and ω is the angular frequency of the acoustic field. As an example, using air as the fluid medium and a frequency of 30 kHz (the conditions for this work), $\delta \sim \mathcal{O}(10\,\mu\text{m})$. For particle diameters comparable to or smaller than δ, the viscosity of the fluid must be considered due to the presence of boundary layers and the effect of streaming around the particle.

The effect of viscosity on the acoustic radiation force has been considered by Doinikov,[29] Danilov and Mironov,[30] and Settnes and Bruus.[31] The equations for the acoustic radiation force of a plane standing wave developed by these authors are lengthy, however, they all share the following general functional form:

$$F_{ar} = C\Phi k d^3 E_{ac} \sin(2kz), \tag{2}$$

where F_{ar} is the acoustic radiation force generated by a plane standing wave on a particle, z is the position on the central axis of the ultrasonic standing wave field, E_{ac} is the acoustic energy density, d is the particle diameter, k is the wave number, $k = 2\pi/\lambda$, where λ is the acoustic wavelength, Φ is a complex function that depends on the material properties of the particle and the surrounding fluid medium, the particle size and the frequency of the standing wave, and C is a constant. The quantities in Eq. (2) that differ between the three aforementioned theories are C and the expression for Φ. Equation (2) can be modified to create a dimensionless acoustic radiation force $\mathcal{F}$ as follows:

a)Electronic mail: jsaylor@clemson.edu

$$\mathcal{F} = \frac{F_{ar}}{\sin(2kz)E_{ac}A}, \tag{3}$$

where A is the particle cross-sectional area, $A = \pi d^2/4$. The utility of Eq. (3) is that $\mathcal{F}$ is independent of the energy density of the standing wave field and the position of the particle in the field; it only depends on the material properties of the particle and the surrounding fluid medium, the particle size, and the frequency of the standing wave.

We note that in addition to the work of Doinikov,[29] Danilov and Mironov,[30] and Settnes and Bruus,[31] other viscous theories and corrections to the acoustic radiation force exist, including the work of Yasuda and Kamakura[32] which included experimental results on polystyrene latex (PSL) particles, Annamalai *et al.*[33] for an elastic particle in a compressible medium, and Asaki and Marston[11] which was applied to bubbles driven above resonance. For simplicity, we focus here on the work of Doinikov,[29] Danilov and Mironov,[30] and Settnes and Bruus[31] when illustrating the presence/absence of a sign change.

It is useful to create a dimensionless particle diameter, d_0, defined as

$$d_0 = \frac{d}{\delta}. \tag{4}$$

The utility of d_0 is that it simplifies identification of conditions where the acoustic radiation force depends on viscosity, i.e., when $d_0 \lesssim 1$. Also, as will be shown below, the theories of Doinikov[29] and Danilov and Mironov[30] only apply for specific ranges of d_0 and plots of $\mathcal{F}$ are therefore typically presented against d_0 to facilitate comparison.

Figure 1 is a plot of $\mathcal{F}$ versus d_0 for the theories of Doinikov,[29] Danilov and Mironov,[30] and Settnes and Bruus.[31] We note in passing that the error in Settnes and Bruus[31] shown in Marston[34] is for the traveling wave limit and does not affect what is presented here for standing waves. The theories of Doinikov[29] and Settnes and Bruus[31] exhibit reasonable agreement for $d_0 > 1$ (the theory by Danilov and Mironov[30] does not extend above $d_0 = 1$), where the theories are well-studied and where experimental data has been obtained and used to validate them.[35] However, for $d_0 < 1$, predictions of $\mathcal{F}$ deviate significantly among these three theories in magnitude and/or sign. In this range of d_0, the theories of Doinikov[29] and Danilov and Mironov[30] predict a change in the sign of $\mathcal{F}$ as d_0 decreases, as shown in Fig. 1. Negative values cannot be plotted on the log-log coordinates of Fig. 1 and so arrows are used to indicate regions of different sign. Here, we define d_c and d_{c0} as the dimensional and dimensionless diameters at which the sign change occurs, respectively. The diameter at which a sign change occurs for the theory of Danilov and Mironov[30] is $d_{c0} = 0.26$. The gap in Doinikov's[29] theory is due to the fact that it only applies for $d_0 \ll 1$ and $d_0 \gg 1$. Hence, though there is obviously a change in sign for $\mathcal{F}$ in this theory, assigning a value for d_{c0} is not possible. On the other hand, there is no sign change predicted by the theory of Settnes and Bruus.[31] For the case of a standing wave field which is considered here, a change in the sign of $\mathcal{F}$ means that the stable position for the particle or drop shifts from the pressure node (velocity anti-node) to the pressure anti-node (velocity node) or vice versa depending on the material properties of the particle and the surrounding fluid.

The uncertainty in whether $\mathcal{F}$ changes sign with particle diameter is a significant gap in the current state of understanding of the acoustic radiation force. A schematic illustration shows the consequences of a unipolar $\mathcal{F}$ in Fig. 2(a) and a bipolar $\mathcal{F}$ in Fig. 2(b). This figure shows a plane standing wave field generated between a transducer and a reflector combination separated by two half wavelengths, which results in the formation of a pressure node and two pressure anti-nodes. If the sign of $\mathcal{F}$ is independent of the particle size, then as Fig. 2(a) shows, all particles will accumulate at the pressure node, regardless of their size (as long as they have the same material properties such as density and compressibility). If the sign of $\mathcal{F}$ is dependent on the particle size (the bipolar case) then, as Fig. 2(b) shows, even for particles with the same material properties, particles where $d > d_c$ will go to the pressure node and particles where $d < d_c$ will go to the pressure anti-node. We note that in Fig. 2, the particles are located exactly at the node or anti-node. In actuality, any finite size particle will be located slightly below these points due to the gravitational force,[18,36,37] though this displacement would be small for the small diameter particles investigated herein. In addition to

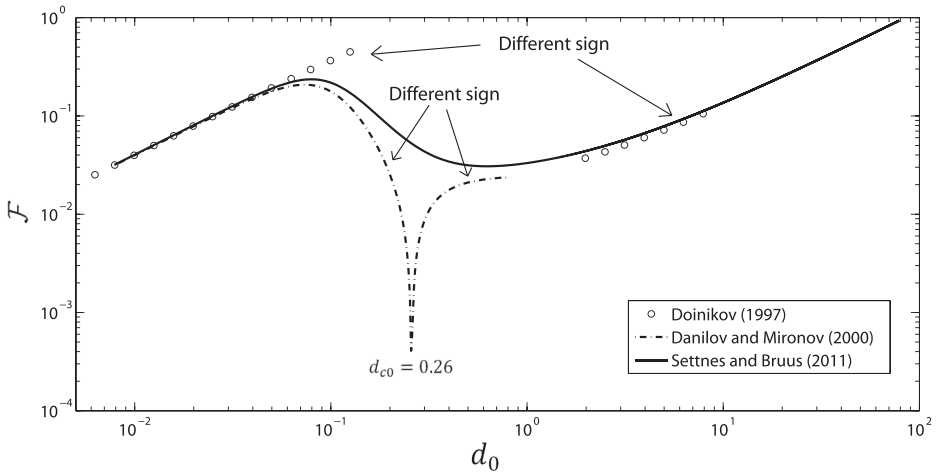

FIG. 1. Dimensionless acoustic radiation force $\mathcal{F}$ on a water drop in a standing wave field predicted by the theories of Doinikov (Ref. 29), Danilov and Mironov (Ref. 30), and Settnes and Bruus (Ref. 31). Arrows indicate where sign changes in $\mathcal{F}$ occur. The frequency is $f = 30$ kHz (that used in the experiments presented herein). The critical non-dimensional diameter at which $\mathcal{F}$ changes sign in the theory of Danilov and Mironov (Ref. 29) is $d_{c0} = 0.26$.

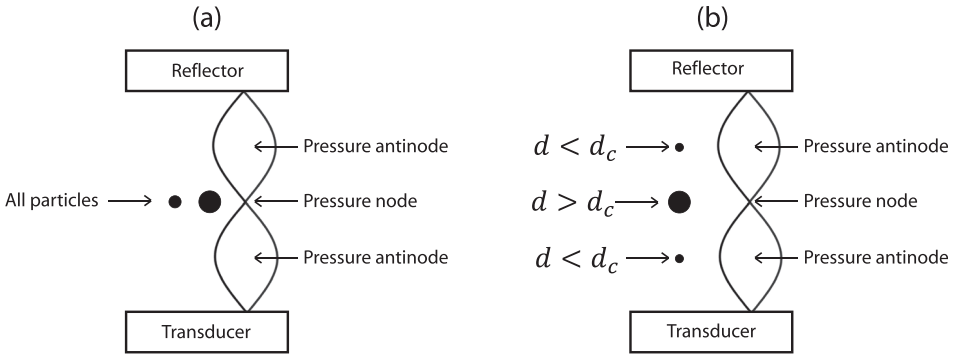

FIG. 2. Schematic illustration showing how a change in the sign of $\mathcal{F}$ affects the location of particles in an ultrasonic standing wave field. (a) The sign of $\mathcal{F}$ is independent of the particle size. (b) The sign of $\mathcal{F}$ is dependent on the particle size. It is noted that in actuality, the objects illustrated in this figure would be located somewhat below the pressure node due to the force of gravity. This has been omitted for clarity.

its basic theoretical importance, the existence of a sign change is significant in applications as well. Just one example concerns particle or cell sorting, where the existence of a sign change may enable simple, effective sorting techniques based on ultrasonics.

There are no experimental studies that we are aware of that prove or disprove any of the three viscous theories presented in Fig. 1 for the range $d_0 < 1$. An experimental study was conducted by Barnkob[35] which validated the theory of Settnes and Bruus[31] down to $d_0 \sim 1$. No sign change was observed in that work. Accordingly, the motivation of the present work is to determine whether a sign change in $\mathcal{F}$ exists and if it does exist, to determine the critical diameter d_c at which it occurs, along with the corresponding non-dimensionalized critical diameter d_{c0}.

II. EXPERIMENTAL METHOD

The heart of the experimental apparatus is illustrated in Fig. 3. The goal of this experimental setup was to (i) generate drops or particles having a variable, controllable diameter, (ii) maintain an ultrasonic standing wave field, and (iii) enable a simple determination of whether the particles or drops ultimately locate at a node or anti-node of the standing wave field. The setup is composed of an ultrasonic transducer reflector combination where the ultrasonic transducer had a resonant frequency ~30 kHz at room temperature (the actual resonant frequency varied from experiment to experiment and was determined by tuning the apparatus, as described below). A standing wave field was achieved by tuning the distance between the transducer and the reflector to an integer number of half wavelengths. In these experiments multiple half wavelengths were used (seven half wavelengths for most of the work presented here), unlike the schematic illustration presented in Fig. 2 where only one node and two anti-nodes were presented for the sake of simplicity.

Referring to Fig. 3, to the left of the standing wave field is a slit nozzle which was used to flow airborne particles into the region of the standing wave. The velocity at the exit of the nozzle was on the order of 10 cm/s. The direction of the flow was oriented perpendicular to the direction of the primary acoustic radiation force, so that the aerodynamic drag force on the particle would not compete with the primary

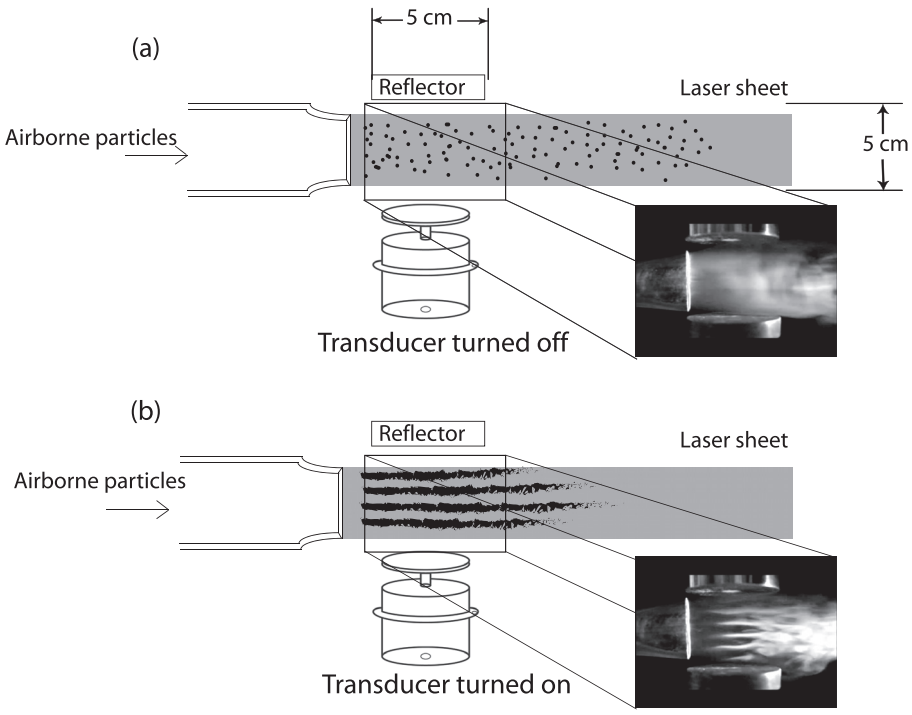

FIG. 3. Experimental setup for determining a possible change in the sign of $\mathcal{F}$ with particle diameter: (a) transducer turned off and (b) transducer turned on.

acoustic radiation force acting on the particle (the acoustic force in the lateral direction is estimated to be orders of magnitude smaller than the primary acoustic force, so its effect was not considered here[38]). The beam of a HeNe laser was formed into a sheet and directed into the ultrasonic standing wave field from the right, thereby illuminating particles in the field. The sheet had a height slightly smaller than the distance between the transducer and reflector; the laser sheet was positioned so that it contained the axis going through the center of the ultrasonic standing wave field. As shown in Fig. 3(a) when the transducer is turned off, the particles are distributed uniformly through the region between the transducer and the reflector without any organized pattern. When the transducer is on and properly tuned, the particles are organized by the standing wave field into a striped pattern as shown in Fig. 3(b). By flowing particles with the same material properties but progressively smaller diameter, a change in the sign of $\mathcal{F}$ would result in a one-quarter wavelength shift in the striped pattern, in the z-direction. That is, as the particle size is decreased, a bipolar $\mathcal{F}$ will result in the particles forming stripes that shift from the nodal locations to the anti-nodal locations. Three different types of particles were used in these experiments: PSL microspheres, fine water drops, and smoke particles. The characteristics are now presented of each of these aerosols along with the experimental apparatus used for each of the three.

The experimental apparatus used to study PSL particles is presented in Fig. 4. The PSL microspheres (Spherotech, Inc.) were monodisperse and had diameters of 0.9, 1.3, 1.7, 2.8, 4.2, and 4.5 μm. These particles were procured as hydrosols that were first diluted in distilled water, then centrifuged and washed to remove any soluble impurities. The resulting diluted hydrosol was then sonicated to disperse any agglomerated PSL particles. As shown in Fig. 4 the diluted hydrosol was atomized into a mist using a TSI model 9302 atomizer. Filtered house air having a relative humidity of 5% was used

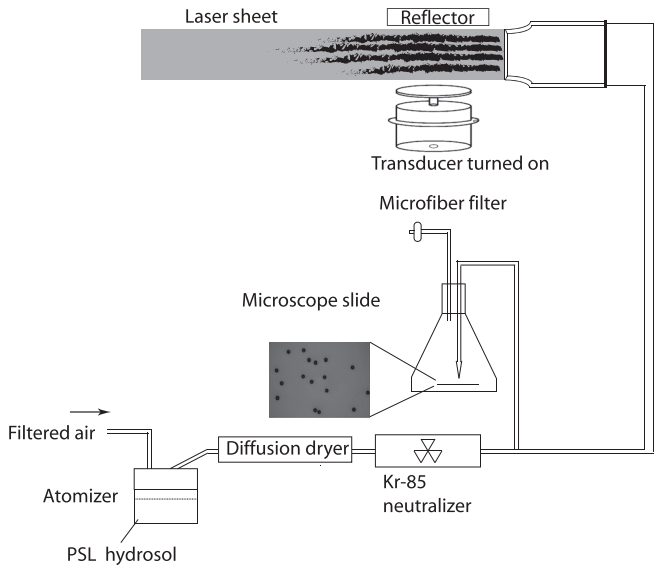

FIG. 4. Configuration of the experimental setup used to disperse and test PSL particles.

to convect the mist through the experimental apparatus and out of the slit nozzle. The dry air alone did not evaporate all of the water surrounding the PSL spheres; to ensure that all water was removed, the flow was passed through a diffusion dryer (ATI DD 250) to remove any remaining moisture. To further ensure that the water surrounding the PSL particles was completely removed, experiments were first conducted using the TSI atomizer, but without any PSL particles in solution. A long exposure image of the flow going through the ultrasonic standing wave field was then obtained. These images showed no reflected laser light, proving that the liquid had indeed been completely removed. Further discussion of the imaging process is presented in Sec. II A below. A TSI model 3012 neutralizer was used to eliminate any possible particle charging; prior research has shown that PSL aerosols formed by atomization of a hydrosol can contain significant static charge.[39]

The particle size distribution (PSD) of the PSL particles was measured using a Leica (DM750) microscope. First, particle samples were collected by directing a portion of the airflow just downstream of the neutralizer onto a glass microscope slide as shown in Fig. 4. Particles on the microscope slide were imaged using a digital camera (Canon DS126291) mounted on the microscope. Images were obtained at random locations on each microscope slide. A fine scaled rule was used to calibrate the images to obtain a micron/pixel conversion to determine the particle diameters from the digital images. An image processing algorithm was developed to obtain the diameter of each of the particles in each image and to generate the PSDs shown in Fig. 5. Further details can be found in our earlier work.[10] Figure 5 shows the expected peaks in particle diameter. Especially important is the absence of particles at multiples of the main peak, showing that particle agglomeration is not a concern.

The second type of particles used were fine water drops generated by an ultrasonic fog generator. The apparatus used for these experiments is illustrated in Fig. 6. The frequency of the ultrasonic fog generator was $f \sim 2$ MHz. Interaction of the acoustic field of the fog generator with the main transducer is expected to be negligible since they were separated by approximately one meter and the attenuation coefficient in air at $f \sim 2$ MHz is on the order of 10^2 dB/m,[40] which corresponds to an attenuation factor of 10^{10} at 1 m distance. The drop diameters obtained from the fog generator are obtained from the equation due to Lang,[41]

$$d_d = 0.34\left(\frac{8\pi\sigma}{\rho f^2}\right)^{1/3}, \tag{5}$$

where σ is the liquid surface tension and ρ is the liquid density. Equation (5) is valid for conditions where the drops are generated from a thin liquid film that covers the ultrasonic nebulizer and where the resulting capillary waves emit drops at their peaks. Use of Eq. (5) presumes that the alternative cavitation mechanism of drop formation is not occurring, which is a reasonable assumption for this low power nebulizer.[42] For water at 22 °C, and $f \sim 2$ MHz, Eq. (5) gives $d_d \sim 1$ μm.

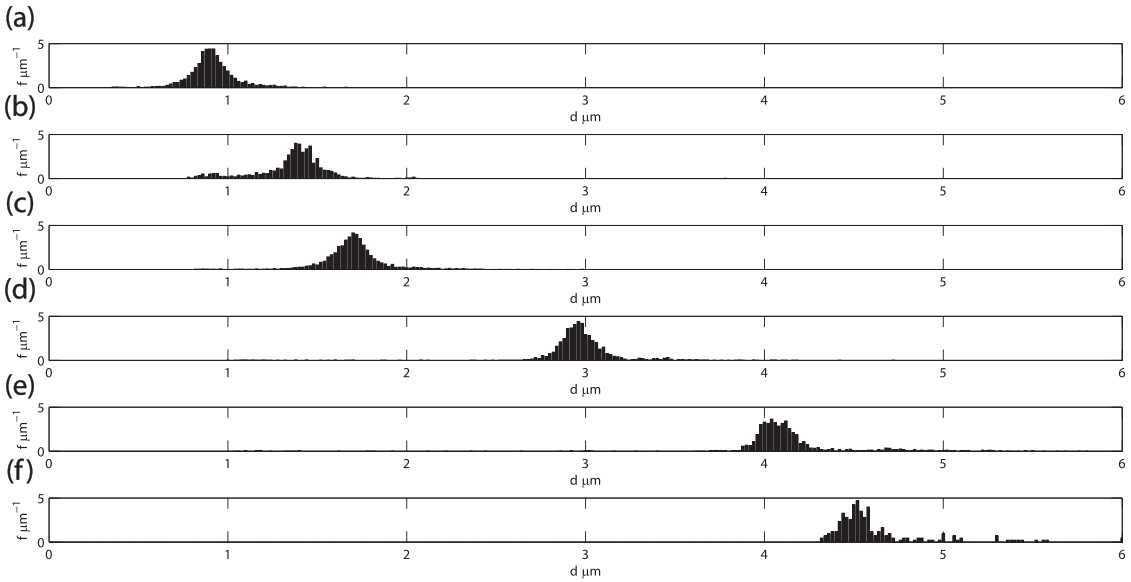

FIG. 5. PSDs for the six PSL particle solutions used. The average values plus/minus one standard deviation were (a) 0.9±0.2 μm, (b) 1.3±0.5 μm, (c) 1.7±0.2 μm, (d) 2.8±0.2 μm, (e) 4.2±0.4 μm, and (f) 4.5±0.5 μm.

In order to vary d_d, the drops generated by the ultrasonic fog generator were fed into a condensation loop as shown in Fig. 6, before they were directed into the standing wave field. The condensation loop consisted of a system of copper tubes submerged in a constant temperature bath. Moist air with a relative humidity of 90% was used to drive the drops though the copper tubes of the condensation loop. By changing the temperature of the constant temperature bath, the amount of water that condensed onto the drops was varied, thus permitting variation and control of d_d. The diameter of the resulting fog drops was measured using a method similar to that used to measure the PSL particles. First, the ultrasonic fog generator in Fig. 6 was used to atomize a solution of disodium fluorescein salt, a fluorescent green dye. The resulting drops were directed onto a glass microscope slide, leaving green drop impact patterns. The microscope and image processing algorithm described earlier was used to measure the diameter of these impact patterns; these are presented in Table I for each of the three water bath temperatures explored. Some difference is expected between the impact pattern diameters and the actual drop diameter since the impact diameters are of a sessile, hemispherically shaped volume of liquid. Research exists relating the diameter of a sessile drop to the spherical drop that formed it. For example, combination of Widom's[43] equations (2) and (4) gives

$$d_d = \frac{d_s}{\sin\theta}\left[\frac{(1+\cos\theta)^2(2-\cos\theta)}{4}\right]^{1/3}, \tag{6}$$

where d_s is the diameter of the sessile drop at the substrate and θ is the contact angle between the drop and the substrate. This equation is simply a geometric relationship for the isothermal three phase contact line problem for a drop on a solid surface where the liquid phase is in equilibrium with the vapor in the gas phase above. Hence, all of the complexity is lumped into θ, which is a complex function of the drop diameter, the drop impact velocity, the surface tension of the drop and the substrate, and the drop viscosity. This complexity prevented us from obtaining the diameter of these drops precisely, and the obtained drop impact pattern diameters must be viewed as an approximation of the actual drop diameter. However, if we assume that θ does not exhibit values close to 0° or 180° (unlikely for water on glass), then d_d and d_s should not deviate significantly from each other and should be monotonic functions of each other, which is sufficient to draw the conclusions made herein.

The third type of particles used in these experiments were smoke particles, generated using the apparatus shown in Fig. 7. Cigarettes and incense sticks were used as the source of the smoke, and these were burned inside a sealed

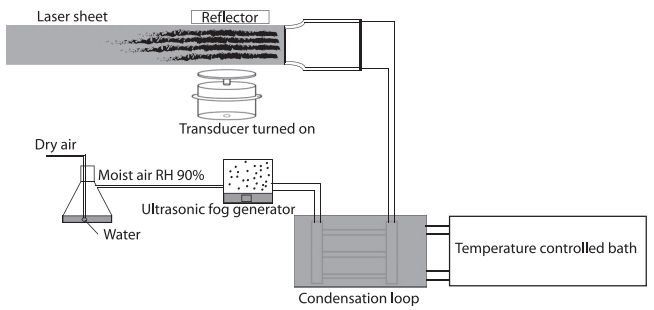

FIG. 6. Portion of the experimental setup used to generate and test micron scale water drops.

TABLE I. The average diameter of drop impact pattern as a function of the temperature of the water bath.

Water bath temperature (°C)	Average diameter (μm)	95% confidence interval (μm)
22	2.722	0.007
12	3.060	0.009
2	4.629	0.012

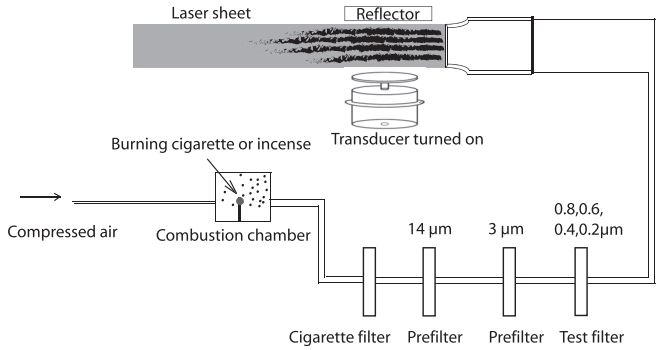

FIG. 7. Portion of the experimental setup used to generate and test smoke particles.

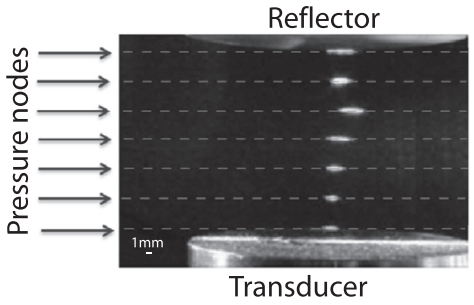

FIG. 8. Position of the pressure nodes as illustrated by millimeter scale drops. These drops were formed by the agglomeration of smaller fine water drops that were introduced into the standing wave field. Blurring exists due to the long (30 s) exposure time.

combustion chamber with a single inlet and outlet. Of course this results in the formation of a broad PSD. To address this we used a sequence of particle filters to pass only those smoke particles smaller than a selected diameter. In this way, by moving to particle filters having a progressively smaller cut-off diameter, we sought to identify a filter diameter at which we saw a shift in the location of the particles in the ultrasonic standing wave field. Dry, filtered, compressed air was used to convect the smoke through the filters. To prevent clogging of the cut-off filters, a cigarette filter and two prefilters with pore size of 14 and 3 μm, respectively, were placed upstream of the cut-off filter. The remaining fine particles were put through the cut-off filter that determined the upper bound in diameter of smoke particles which were allowed to enter the ultrasonic standing wave field. Experimental runs were conducted using four different cut-off filters having pore sizes $d_f = 0.8$, 0.6, 0.4, and 0.2 μm. The prefilters and the test filters were polycarbonate membrane disk filters (Sterlitech) which are manufactured for particulate analysis and have precisely controlled pore sizes.

A. Procedure

Before each experiment the frequency of the alternating current (ac) voltage applied to the transducer was tuned by attaching a piezoelectric sensor to the back of the transducer and monitoring its feedback on an oscilloscope. The frequency of the ac signal was tuned until the amplitude of the feedback signal from the piezoelectric sensor reached a maximum, indicating that the transducer was vibrating at its resonance frequency. After that, the gap distance between the horn of the transducer and the reflector was tuned so that this distance was an integer number of half wavelengths, which is needed to form a standing wave between the gap. This was done by introducing a fine water spray, and adjusting the gap distance until the fine spray drops accumulated in the pressure nodes, and agglomerated into millimeter scale drops, instead of simply falling downward (this also enabled us to identify the location of the pressure nodes, as described below). The laser sheet shown in Fig. 3 was then turned on. A Canon digital camera (model DS126311) was oriented with its optical axis normal to the laser sheet. At the beginning of each experiment images were obtained of the aforementioned millimeter scale drops to ensure that the camera was focused on the plane of the laser sheet. An example of such an image is presented in Fig. 8. The exposure time of the image was set to 30 s to make sure only the time-averaged positions of these drops were recorded.

For millimeter sized water drops in an ultrasonic standing wave field, the theories of Doinikov[29] and Settnes and Bruus[31] agree with each other and so the positions of these large drops can be confidently identified as residing in the pressure nodes. So by recording images of the positions of these drops in the standing wave field, the locations of the pressure nodes are also recorded. Once the positions of the pressure nodes are recorded, particles of progressively smaller diameters were introduced into the field and their stable locations compared with the locations of the pressure nodes.

The above approach was taken for all three particle types investigated. Specifically, for the micron-scale water drops, the temperature of the constant temperature water bath shown in Fig. 6 was increased (decreased) to create smaller (larger) drops. Images documenting the location of the drops for each water bath temperature were recorded. For PSL particles, images were acquired for each of the six PSL particle diameters investigated (Fig. 5). For the case of the smoke particles, images were acquired for each of the four test filter pore diameters utilized. In all cases, the number densities of the particles/drops were low and visualization required long time exposures; typical exposure times ranged from 10 to 30 s.

III. RESULTS

Figure 9 presents an image from a sample run where fog drops were used. Figure 9(a) presents an image of the fog generator drops as they travel through the standing wave field, while Fig. 9(b) presents an image of the millimeter scale drops in the same standing wave. It is clear that these two very different sized drops accumulate in different locations in the ultrasonic standing wave field. The millimeter scale drops are located at the pressure nodes, and the micron scale drops went to the pressure anti-nodes. The fog drops seen in Fig. 9(a) were generated without using the condensation loop and therefore are the smallest drops that could be generated by that facility. Because the only difference between the two sets of drops presented in Fig. 9 is their diameter (they are both water obtained from the same source and hence have precisely the same properties), these results

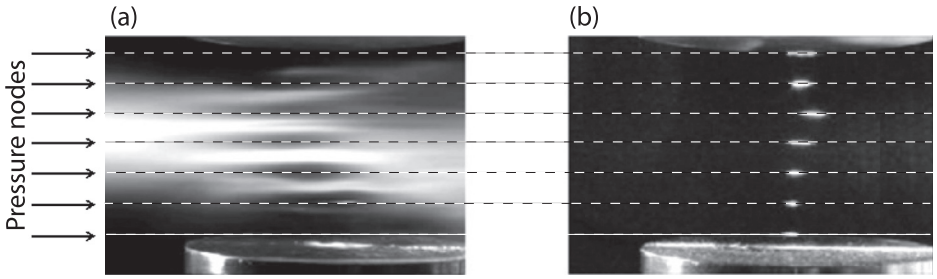

FIG. 9. Positions of the micron scale (a) and millimeter scale (b) water drops in an ultrasonic standing wave field.

show that the sign of $\mathcal{F}$ is indeed dependent on the particle size, though we describe facets of the experimental method that could conceivably compromise this conclusion in Sec. IV. Presuming for the moment that a sign change does exist, the next step is to measure the critical diameter d_c at which $\mathcal{F}$ changes sign.

The results obtained using the condensation loop apparatus (Fig. 6) are presented in Table II and Fig. 10. As noted in Sec. II, as the temperature of the water bath is reduced, more condensation occurs and the drop diameter increases. As shown in Table II and Fig. 10, for water bath temperatures $<2\,^{\circ}$C, the resulting fog drops were located in the nodes of the standing wave field [Fig. 10(a)] while for water bath temperatures ranging from $10\,^{\circ}$C to $22\,^{\circ}$C, the drops were located in the anti-nodes [Fig. 10(c)]. For water bath temperatures between $2\,^{\circ}$C and $10\,^{\circ}$C, the location of the drops is ambiguous as shown in Fig. 10(b) which shows a generally diffuse image without the clear bands seen in Figs. 10(a) and 10(c). These results indicate that the critical diameter d_c at which the sign of $\mathcal{F}$ changes lies within the range of drop diameters that are created by the drop generator apparatus (Fig. 6) when the condensation loop temperature ranges from $3\,^{\circ}$C to $9\,^{\circ}$C.

As noted in Sec. II, relating the water bath temperature of the condensation loop apparatus to the drop diameter is challenging. Using the data presented in Tables I and II, the transition from nodes to anti-nodes occurs for a range of drop impact pattern diameters ranging from 3.1 to 4.6 μm, and so we estimate $3.1\,\mu\text{m} < d_c < 4.6\,\mu\text{m}$, which corresponds to $0.24 < d_{c0} < 0.35$. However, as pointed out in Sec. II, the drop impact pattern diameter is an approximation of the actual drop diameter. In most cases the drop impact pattern diameter is bigger than the actual drop diameter due to the spread of the drop on the substrate surface. Hence, to be conservative, we claim based on just these data that $d_c < 4.6\,\mu$m and $d_{c0} < 0.35$.

Translating the water bath temperatures into drop diameters more accurately would result in a more precise d_c. This could be obtained using a correlation for the mass transfer rate for condensation onto a drop at given values for the drop temperature, air temperature, and relative humidity. These parameters may be estimated, however what is also needed is an accurate value for the number concentration of drops in the condensation loop which we had no method for measuring. Accordingly, the PSL and smoke particle experiments were used to provide a more precise estimate of (d_c, d_{c0}).

TABLE II. Positions of fog drops in the ultrasonic standing wave field as a function of the temperature of the water bath.

Water bath temperature	Location
$10\,^{\circ}$C–$22\,^{\circ}$C	Pressure anti-nodes
$3\,^{\circ}$C–$9\,^{\circ}$C	Ambiguous
$<2^{\circ}$C	Pressure nodes

In one sense PSL particles are ideal for determining d_c since the diameters of these particles are very well characterized, both from the manufacturer's quoted values as well as from our own measurements (see Fig. 5). Unfortunately, as shown in Table III, for all of the PSL particle diameters investigated here the particles were located in the pressure nodes of the ultrasonic standing wave field. Since the pressure nodes are where particles larger than d_c are located, even the smallest PSL diameter investigated here, $d = 0.9$ μm, did not satisfy the condition $d < d_c$. These results suggest that $d_c < 0.9\,\mu$m and $d_{c0} < 0.9\,\mu\text{m}/13\,\mu\text{m} = 0.07$. While these results do not disagree with the results from the condensation loop apparatus, a more definitive result was desired. We considered imaging PSL particles smaller than 0.9 μm, however imaging the 0.9 μm PSL particles was already a challenge due to the small scattered light intensity. Obtaining enough signal to generate an image for even smaller diameters would have required a number density of PSL particles much larger than possible using our atomizer setup. Accordingly, we sought to determine the value of d_c using smoke.

Table IV presents the location of the smoke particles as a function of the pore size of the test filter used in the smoke experiments. As described in Sec. II, incense or cigarette smoke has a broad distribution of particle diameters. By using filters, only particles having diameters smaller than the pore size d_f of the test filter were allowed to enter the ultrasonic standing wave field. Table IV presents the smoke type, filter cut-off diameter and nodal location of smoke accumulation for each of the runs. Referring to the cigarette smoke experiments, runs 3 and 4 show that in the cigarette smoke were particles having a diameter $0.2\,\mu\text{m} < d < 0.4\,\mu$m that went to the pressure nodes (and not to the anti-nodes). Run 4 showed no particles, indicating that virtually all the smoke particles were larger than 0.2 μm. For the incense smoke, runs 7 and 8 reveal that in that smoke were particles having diameters $0.2\,\mu\text{m} < d < 0.4\,\mu$m that went to the anti-nodes and not to the nodes. Like run 4, run 8 showed no particles, also indicating that virtually all the incense particles were larger than 0.2 μm. These two facts taken together indicate that $0.2\,\mu\text{m} < d_c < 0.4\,\mu$m, assuming that the properties of the two types of smoke are the same. These results

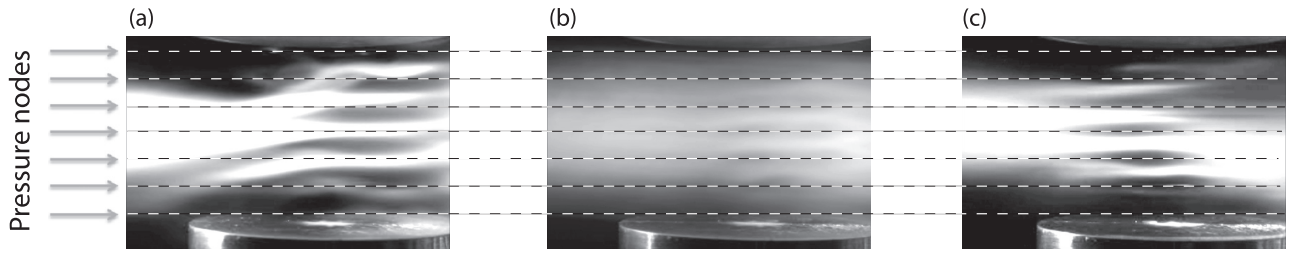

FIG. 10. Positions of the micron scale water drops in an ultrasonic standing wave field for different water bath temperature ranges: (a) <2 °C. (b) 3 °C–9 °C. (c) 10 °C–22 °C.

correspond to $0.015 < d_{c0} < 0.031$, which agrees with the PSL and water drop experiments.

There is the possibility that no particles were observed in runs 4 and 8 due to a simple inability to see the particles of that size with our optical setup. But even if that is true, the above conclusion still holds. This is because in run 3 we showed some particles went through the 0.4 μm filter and were observed in the nodes, but these same particles were not seen in run 4 when the filter size was reduced to 0.2 μm. Even if it was the case that there were other particles that went through the 0.2 μm filter that we could not see, this does not change the fact that particles having diameters $0.2\ \mu\text{m} < d < 0.4\ \mu\text{m}$ went to the pressure nodes and not to the pressure anti-nodes. This same argument holds for runs 7 and 8, validating the conclusion that $0.2\ \mu\text{m} < d_c < 0.4\ \mu\text{m}$.

IV. DISCUSSION

The results presented in Sec. III suggest that the direction of the acoustic radiation force does depend on particle diameter and that the direction changes at $0.015 < d_{c0} < 0.031$. The value of d_{c0} predicted by Danilov and Mironov[30] for water drops is 0.26 (Fig. 1), which is an order of magnitude larger than the results obtained using smoke particles, though in agreement with the broad estimate obtained from our water drop experiments. This discrepancy may be due to the difference in the material properties of water and smoke particles. For the case of the theory of Danilov and Mironov, density would be the property that could cause differences in the predicted d_{c0}.[30] However, as shown in Fig. 11, the theory of Danilov and Mironov indicates that the density of the particle would need to attain values of approximately $\rho = 10^7$ kg/m^3 in order for d_{c0} to reach the values of 0.015–0.031 measured here. Hence this cannot be the source of the discrepancy.

An alternative source of the discrepancy between the results presented here and the theory of Danilov and Mironov[30] concerns fluid viscosity. The theory of Danilov and Mironov[30] assumes a constant fluid viscosity. However, it is known that a particle in an ultrasonic standing wave field can experience a viscosity that varies periodically with the acoustic field due to the periodic adiabatic compression and rarefaction of the acoustic wave.[44,45] According to the results of Czyz[44] this may alter $\mathcal{F}$ as shown in Fig. 12. In Fig. 12 the force predicted by Czyz[44] is presented in dimensionless form as $\mathcal{F}_{vis}$ [obtained using Eq. (3)]. Unfortunately, it is not clear how to use $\mathcal{F}_{vis}$ to correct $\mathcal{F}$. One could simply add $\mathcal{F}_{vis}$ to $\mathcal{F}$, however this is not likely to yield a meaningful result due to the potentially complex, nonlinear interactions between the different mechanisms. Further theoretical investigation is needed to understand the interaction between these mechanisms and to determine the combined force generated by them.

It is known that the very presence of particles in an ultrasonic standing wave field can affect that standing wave. Kwiatkowski and Marston[46] studied aqueous solutions of hollow glass spheres and polystyrene-divinylbenzene microspheres and found that the natural frequency of their chamber shifted as the particles migrated to the pressure nodes. This was found to be significant for particle volume fractions as small as 0.001. Similar observations were made by Hammarström *et al.*[47] It is theoretically possible that the results observed here could be influenced by this effect. In other words, it is possible that as particles were introduced into the standing wave field, the resonant frequency of the chamber changed enough to shift the accumulation zones a quarter wavelength in value. To know if this was indeed the case would require the number density of the particles used in our experiments. We have such a number density, but only for the case of the 0.9 μm PSL particles, having not anticipated the need for this data at the time of these experiments (furthermore, the laser particle counter we had access

TABLE III. Positions of PSL particles in the ultrasonic standing wave field as a function of the particle diameter.

Diameter (μm)	Position
4.5±0.5	Pressure nodes
4.2±0.4	Pressure nodes
2.8±0.2	Pressure nodes
1.7±0.2	Pressure nodes
1.3±0.5	Pressure nodes
0.9±0.2	Pressure nodes

TABLE IV. Positions of smoke particles in the ultrasonic standing wave as a function of filter pore size. "None" means no particles were observed.

Run	Smoke type	d_f (μm)	Position
Run 1	Cigarette smoke	0.8	Pressure nodes
Run 2	Cigarette smoke	0.6	Pressure nodes
Run 3	Cigarette smoke	0.4	Pressure nodes
Run 4	Cigarette smoke	0.2	None
Run 5	Incense smoke	0.8	Pressure anti-nodes
Run 6	Incense smoke	0.6	Pressure anti-nodes
Run 7	Incense smoke	0.4	Pressure anti-nodes
Run 8	Incense smoke	0.2	None

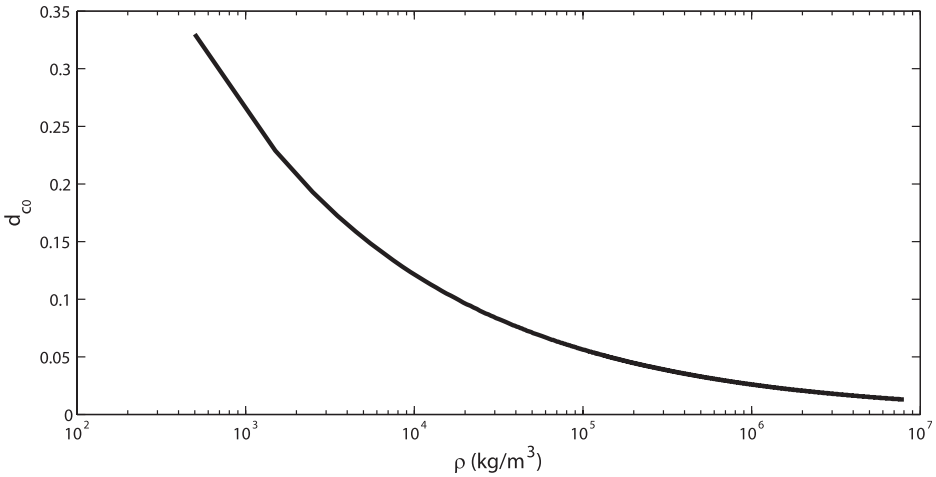

FIG. 11. The dimensionless critical particle diameter d_{c0} as a function of particle density ρ as predicted by the theory of Danilov and Mironov (Ref. 29). The frequency of the standing acoustic wave field was 30 kHz and the surrounding fluid was air, the same as for the experiments presented here.

to was not capable of sizing particles smaller than 0.5 μm). For these 0.9 μm PSL particles, the particle number density was $N = 192/\text{cm}^3$, which gives a particle volume fraction of 7×10^{-11}, which is seven orders of magnitude smaller than that used in the work of Kwiatkowski and Marston.[46] We note that we were able to get images of particles in the ultrasonic standing wave field at this low number density, only by resorting to long exposure times, ranging from 10 to 30 s.

It is unlikely that the location of the accumulation zones in our experiments was affected by the number density of the particles since the theory developed by Kwiatkowski and Marston[46] predicts that the relative deviation of the resonant frequency scales with the particle volume fraction. However, to show that the volume fractions were very low for all of the particle types and particle diameters presented here would require the number densities of those particles as well which, as noted above, we did not measure. Nevertheless, an estimate is possible. Several aspects of our imaging setup remained constant during all experiments, namely, the wavelength of the laser (633 nm), the intensity of that laser and the distance and orientation of the camera with respect to the image plane. For these experiments, the particle diameters fall into the Mie scattering regime.[48] In this situation, if we assume that the pixel intensity is proportional to the scattering cross section of the particle and the number density of those particles, then the number density N of any of our runs can be obtained according to

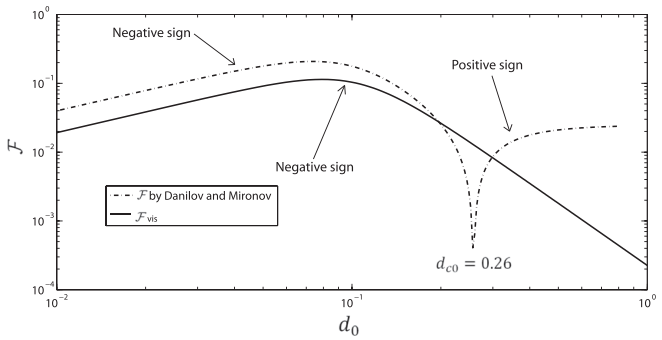

FIG. 12. Comparison between $\mathcal{F}$ on a water drop for a standing wave field at $f = 30$ kHz in air as predicted by Danilov and Mironov (Ref. 29) and due to the change in ν predicted by Czyz (Ref. 43). Arrows indicate regions where the sign of $\mathcal{F}$ is different.

$$\frac{N}{N_{0.9}} = \frac{P}{P_{0.9}} \frac{[\sigma A_c t_e \text{ISO}]_{0.9}}{\sigma A_c t_e \text{ISO}}, \tag{7}$$

where P is the pixel intensity, A_c is the aperture area of the camera, σ is the particle scattering coefficient, t_e is the exposure time, and ISO is the camera's ISO setting. The subscript 0.9 refers to the 0.9 μm PSL particle case where the number density was recorded. Equation (7) assumes that the pixel intensity is proportional to ISO and A_c. In Eq. (7), the values for A_c, t_e, and ISO were recorded for each experiment and therefore were knowns. Values of σ were obtained from van de Hulst.[49] The pixel intensity was obtained by averaging a small group of pixels in the accumulation zone and where the image intensity was maximum. The diameter used to obtain σ was obtained from Fig. 5 for the PSL particles, from Table I for the fog drops, and using the test filter diameter for the smoke experiments. Using Eq. (7) and all of the above assumptions gave the following maximum number densities for each of the particle types studied. For cigarette smoke particles, the maximum was $N = 603/\text{cm}^3$ at $d = 0.6$ μm; for incense particles, the maximum was $N = 1623/\text{cm}^3$ at $d = 0.4$ μm; for PSL particles, the maximum was $N = 192/\text{cm}^3$ at $d = 0.9$ μm (this is a measurement, as noted above); for fog drops, the maximum was $N = 3768/\text{cm}^3$ at $d = 4.6$ μm. For all cases, the maximum volume fraction was 1.9×10^{-7} which was for the case of the water drops under the conditions shown in Fig. 10(a). The computed volume fractions for the smoke or PSL runs at any diameter were smaller than this value; the overwhelming majority of the runs had volume fractions in the 10^{-11} to 10^{-10} range. Hence, the maximum volume fraction observed herein is more than three orders of magnitude smaller than that investigated in Kwiatkowski and Marston,[46] where relative frequency shifts on the order of 100 Hz were observed for a nominal resonant frequency of 833 kHz. If the relative frequency shift is linearly related to the volume fraction, as shown by those authors, then the frequency shift for the present work should be only a few Hz, which would not cause the kind of change in nodal structure observed herein.

We note that N for the 0.9 μm PSL particle case were measured at the exit of the slit nozzle (the number density in the volume between the transducer and reflector could not be measured without disturbing the standing wave field).

Hence, the computed number densities presented above are for that location as well. The number density, upon entering the field, will be increased by the acoustic radiation force which will concentrate them in the nodes, while the number density will be decreased as the slit jet formed by the nozzle (Fig. 3) diffuses outward (in the direction normal to the image plane). It is difficult to know the number density that would exist within the field. However, due to the competing effects of concentration and diffusion, we do not expect an order of magnitude deviation from the values cited above.

Another point of concern in interpreting the experiments presented herein is that the fluid properties of pure air were used when computing any required parameters, such as for the kinematic viscosity used in computing δ and d_0, for example. This could be a problem at high particle densities where the particle laden air effectively becomes a gas having very different properties than air. This can be significant as shown in the work of Tuckermann *et al.*[50] who show how introducing gases of different properties into a standing wave field results in the segregation of that gas in the nodes of the field. Such effects are unlikely herein since the very low volume fractions that exist here will not have a significant effect on the effective viscosity, density, etc.

In the analysis and interpretation of results conducted herein, it is assumed that the ultrasonic standing wave field is one-dimensional and that the scattering of sound off of one drop or particle does not impact another drop or particle. Said another way, the sound field experienced by any particle is presumed to be identical to that which would be experienced if no other particles were present. This clearly is not the case here. How to address such a multi-bounce problem is unclear. It is tempting to presume that the low number densities explored here make this effect negligible, but without a theory describing this, such a statement is difficult to make with confidence.

Finally, it is possible that the discrepancy in d_{c0} between our results and the theoretical prediction may be that d_{c0} depends on other particle properties such as compressibility. This is further supported by the fact that other theories for F_{ar}, though they do not predict d_{c0}, do use compressibility in their predictions of F_{ar}.[25,29,31] A consequence of this possibility is that the value of d_{c0} presented in this experimental work may not be applicable to particles having compressibilities different from that of water particles and smoke particles. Further theoretical and experimental investigation is needed to find a value for d_{c0} valid for all particle types.

V. CONCLUSION

The experimental work presented in this paper suggests that for water drops and smoke particles, the direction of the acoustic radiation force acting on them was bipolar, changing sign when the diameter of these particles were decreased below a critical value. The value of the dimensionless critical diameter for smoke particles was $0.015 < d_{c0} < 0.031$, which differs by an order of magnitude from that predicted by existing theories. This may be due to the compressibility of smoke particles, which we were unable to quantify. However it may also be due to other mechanisms which contribute to the acoustic radiation force not included in existing theories.

ACKNOWLEDGMENTS

This material is based upon work supported by the National Science Foundation under Grant No. 1336632.

[1]B. Hammarstrom, T. Laurell, and J. Nilsson, "Seed particle-enabled acoustic trapping of bacteria and nanoparticles in continuous flow systems," Lab Chip **12**(21), 4296–4304 (2012).
[2]H. Mulvana, S. Cochran, and M. Hill, "Ultrasound assisted particle and cell manipulation on-chip," Adv. Drug Delivery Rev. **65**(11), 1600–1610 (2013).
[3]J. Wu, "Acoustical tweezers," J. Acoust. Soc. Am. **89**(5), 2140–2143 (1991).
[4]J. R. Gao, C. D. Cao, and B. Wei, "Containerless processing of materials by acoustic levitation," Adv. Space Res. **24**(10), 1293–1297 (1999).
[5]J. K. Weber, D. S. Hampton, D. R. Merkley, C. A. Rey, M. M. Zatarski, and P. C. Nordine, "Aero-acoustic levitation: A method for containerless liquid-phase processing at high temperatures," Rev. Sci. Instrum. **65**(2), 456–465 (1994).
[6]R. R. Whymark, "Acoustic field positioning for containerless processing," Ultrasonics **13**(6), 251–261 (1975).
[7]X. Ding, S. C. S. Lin, M. I. Lapsley, S. Li, X. Guo, C. Y. Chan, I. K. Chiang, L. Wang, J. P. McCoy, and T. J. Huang, "Standing surface acoustic wave (SSAW) based multichannel cell sorting," Lab Chip **12**(21), 4228–4231 (2012).
[8]I. González, L. J. Fernández, T. E. Gómez, J. Berganzo, J. L. Soto, and A. Carrato, "A polymeric chip for micromanipulation and particle sorting by ultrasounds based on a multilayer configuration," Sens. Act. B: Chem. **144**(1), 310–317 (2010).
[9]S. Kapishnikov, V. Kantsler, and V. Steinberg, "Continuous particle size separation and size sorting using ultrasound in a microchannel," J. Stat. Mech.: Theory Exp. **P01012**, 1–15 (2006).
[10]W. Ran, J. R. Saylor, and R. G. Holt, "Improved particle scavenging by a combination of ultrasonics and water sprays," J. Aerosol Sci. **67**, 104–118 (2014).
[11]T. J. Asaki and P. L. Marston, "Acoustic radiation force on a bubble driven above resonance," J. Acoust. Soc. Am. **96**, 3096–3099 (1994).
[12]B. T. Chu and R. E. Apfel, "Acoustic radiation pressure produced by a beam of sound," J. Acoust. Soc. Am. **72**(6), 1673–1687 (1982).
[13]R. G. Holt and L. A. Crum, "Acoustically forced oscillations of air bubbles in water: Experimental results," J. Acoust. Soc. Am. **91**(4), 1924–1932 (1992).
[14]P. L. Marston and R. E. Apfel, "Acoustically forced shape oscillation of hydrocarbon drops levitated in water," J. Colloid Interface Sci. **68**, 280–286 (1979).
[15]S. L. Min, R. G. Holt, and R. E. Apfel, "Simulation of drop dynamics in an acoustic positioning chamber," J. Acoust. Soc. Am. **91**(6), 3157–3165 (1992).
[16]Y. Tian, R. G. Holt, and R. E. Apfel, "Deformation and location of an acoustically levitated liquid drop," J. Acoust. Soc. Am. **93**, 3096–3104 (1993).
[17]E. H. Trinh and C. J. Hsu, "Acoustic levitation methods for density measurements," J. Acoust. Soc. Am. **80**(6), 1757–1761 (1986).
[18]E. H. Trinh, Marston, P. L., and J. L. Robey, "Acoustic measurement of the surface tension of levitated drops," J. Colloid Interface Sci. **124**(1), 95–103 (1988).
[19]E. H. Trinh and J. L. Robey, "Experimental study of streaming flows associated with ultrasonic levitators," Phys. Fluids **6**, 3567–3579 (1994).
[20]M. A. H. Weiser and R. E. Apfel, "Extension of acoustic levitation to include the study of micron-size particles in a more compressible host liquid," J. Acoust. Soc. Am. **71**(5), 1261–1268 (1982).
[21]X. Yang, R. A. Roy, and R. G. Holt, "Bubble dynamics and size distributions during focused ultrasound insonation," J. Acoust. Soc. Am. **116**(6), 3423–3431 (2004).
[22]L. V. King, "On the acoustic radiation pressure on spheres," Proc. R. Soc. London, Ser. A **147**(861), 212–240 (1934).
[23]L. P. Gor'kov, "On the forces acting on a small particle in an acoustical field in an ideal fluid," Sov. Phys. Dokl. **6**, 773–775 (1962).
[24]K. Yosioka and Y. Kawasima, "Acoustic radiation pressure on compressible sphere," Acustica **5**, 167–173 (1955).
[25]T. Hasegawa and K. Yosioka, "Acoustic-radiation force on a solid elastic sphere," J. Acoust. Soc. Am. **46**(5B), 1139–1143 (1969).

[26]L. A. Crum, "Acoustic force on a liquid droplet in an acoustic stationary wave," J. Acoust. Soc. Am. **50**, 157–163 (1971).
[27]L. D. Landau and E. M. Lifshitz, *Fluid Mechanics*, Vol. 6 of *Course of Theoretical Physics*, 2nd ed. (Pergamon, New York, 1989).
[28]L. Rayleigh, "On the circulation of air observed in Kundt's tubes, and on some allied acoustical problems," Philos. Trans. R. Soc. London **175**, 1–21 (1884).
[29]A. A. Doinikov, "Acoustic radiation force on a spherical particle in a viscous heat-conducting fluid. I. General formula," J. Acoust. Soc. Am. **101**, 713–721 (1997).
[30]S. D. Danilov and M. A. Mironov, "Mean force on a small sphere in a sound field in a viscous fluid," J. Acoust. Soc. Am. **107**, 143–153 (2000).
[31]M. Settnes and H. Bruus, "Forces acting on a small particle in an acoustical field in a viscous fluid," Phys. Rev. E **85**(1), 016327 (2012).
[32]K. Yasuda and T. Kamakura, "Acoustic radiation force on micrometer-size particles," Appl. Phys. Lett. **71**(13), 1771–1773 (1997).
[33]S. Annamali, S. Balachandar, and M. K. Parmar, "Mean force on a finite-size spherical particle due to an acoustic field in a viscous compressible medium," Phys. Rev. E **89**, 053008 (2014).
[34]P. L. Marston, "Viscous contributions to low-frequency scattering, power absorption, radiation force, and radiation torque for spheres in acoustic beams," POMA **19**, 045005 (2013).
[35]R. Barnkob, P. Augustsson, T. Laurell, and H. Bruus, "Acoustic radiation- and streaming-induced microparticle velocities determined by microparticle image velocimetry in an ultrasound symmetry plane," Phys. Rev. E **86**(5), 056307 (2012).
[36]P. L. Marston and D. B. Thiessen, "Manipulation of fluid objects with acoustic radiation pressure," Ann. N.Y. Acad. Sci. **1027**, 414–434 (2004).
[37]E. H. Trinh and C.-J. Hsu, "Equilibrium shapes of acoustically levitated drops," J. Acoust. Soc. Am. **79**(5), 1335–1338 (1986).
[38]A. Hancock, "Observation of forces on microparticles in acoustic standing waves," Master's thesis, University of California, Davis (2001).
[39]K. T. Whitby and Y. H. Liu, "Polystyrene aerosols-electrical charge and residue size distribution," Atmos. Environ. **2**, 103–116 (1968).
[40]H. E. Bass, L. C. Sutherland, A. J. Zuckerwar, D. T. Blackstock, and D. M. Hester, "Atmospheric absorption of sound: Further developments," J. Acoust. Soc. Am. **97**(1), 680–683 (1995).
[41]R. J. Lang, "Ultrasonic atomization of liquids," J. Acoust. Soc. Am. **34**, 6–8 (1962).
[42]R. Rajan and A. B. Pandit, "Correlations to predict droplet size in ultrasonic atomization," Ultrasonics **39**(4), 235–255 (2001).
[43]B. Widom, "Line tension and the shape of a sessile drop," J. Phys. Chem. **99**(9), 2803–2806 (1995).
[44]H. Czyz, "On the concentration of aerosol particles by means of drift forces in a standing wave field," Acustica **70**(1), 23–28 (1990).
[45]P. J. Westervelt, "The mean pressure and velocity in a plane acoustic wave in a gas," J. Acoust. Soc. Am. **22**, 319–327 (1950).
[46]C. S. Kwiatkowski and P. L. Marston, "Resonator frequency shift due to ultrasonically induced microparticle migration in an aqueous suspension: Observations and model for the maximum frequency shift," J. Acoust. Soc. Am. **103**, 3290–3300 (1998).
[47]B. Hammarström, M. Evander, J. Wahlström, and J. Nilsson, "Frequency tracking in acoustic trapping for improved performance stability and system surveillance," Lab Chip **14**, 1005–1013 (2014).
[48]R. Siegel and J. R. Howell, *Thermal Radiation Heat Transfer* (McGraw-Hill, New York, 1981).
[49]H. C. van de Hulst, *Light Scattering by Small Particles* (Dover, New York, 1982).
[50]R. Tuckermann, B. Neidhart, E. G. Lierke, and S. Bauerecker, "Trapping of heavy gases in stationary ultrasonic fields," Chem. Phys. Lett. **363**, 349–354 (2002).
[51]E. H. Trinh, "Compact acoustic levitation device for studies in fluid dynamics and material science in the laboratory and microgravity," Rev. Sci. Instrum. **56**, 2059–2065 (1985).